Physica Scripta

PAPER

Low SAR ultra compact UWB vivaldi non-uniform slot antennas for breast cancer detection

RECEIVED
23 June 2024

REVISED
23 October 2024

ACCEPTED FOR PUBLICATION
8 November 2024

PUBLISHED
19 November 2024

Sahar Saleh[1,2], **Tale Saeidi**[1,3], **Nick Timmons**[1], **Faroq Razzaz**[4,5] and **Ayman A Althuwayb**[6]

[1] WiSAR Lab, Atlantic Technological University (ATU), Letterkenny, Co. Donegal, F92 YY97, Ireland
[2] Department of Electronics and Communications Engineering, Faculty of Engineering, Aden University, Aden 5243, Yemen
[3] Electrical and Electronics Engineering Department, Faculty of Engineering and Natural, Sciences, Istinye University, Istanbul 34326, Turkey
[4] Electrical Engineering Department, College of Engineering, Prince Sattam Bin Abdulaziz University, Al-Kharj 16278, Saudi Arabia
[5] Faculty of Engineering and Information Technology, Taiz University, Taiz, 6803, Yemen
[6] Electrical Engineering Department, College of Engineering, Jouf University, Sakaka, Aljouf, 72388, Saudi Arabia

E-mail: sahar.saleh@atu.ie

Keywords: ultra-wideband (UWB), exponential non-uniform slot profile antenna (ENSPA) theory, microwave imaging (MI), specific absorption rate (SAR), breast cancer detection (BCD)

Abstract

Breast cancer is one of the growing issues among women. Current ultrawideband (UWB) antennas utilized for Microwave Imaging (MI) present several limitations, such as resolution and penetration trade-offs, large dimensions of the antennas degrade patient comfort, and clutter in the received signal. To tackle these restrictions, this study presents the design, fabrication, and testing of ultra-compact Vivaldi antennas based on the new Vivaldi non-uniform slot profile antenna (VNSPA) theory. These antennas, with their significant slot length reductions of 50 % and 60 %, and circuit area reductions of 72.74 % (Antenna A) and 81.8 % (Antenna B), hold great promise for modern wireless communication and medical fields. Antenna A and B provide matching S_{11} values of less than −11.36 dB and −10.21 dB and peak gains of 5.9 dBi and 6 dBi through 2.63–12.33 GHz and 3.16–14.34 GHz, respectively. Although Antenna B is 30.58 % smaller than Antenna A, it provides 13.24 % bandwidth (BW) with a 1.7 % gain enhancement, highlighting the significance of the exponential nonuniform slot profile (ENSP) shape on the antenna's performance. Antenna B provides good Breast Cancer Detection (BCD) results through UWB MI. The simulation in this work, which is performed using computer simulation technology (CST) software, agrees well with the practical results to prove the antenna's capabilities in detecting tumors in a breast. These results, like the directive stable radiation patterns and low specific absorption rate (SAR) values, ensure the proposed antennas are good candidates for modern wireless communication applications such as reader antennas in body area networks and high-resolution medical applications such as BCD.

1. Introduction

In today's wireless communication system, where everything is connected, efficient and small RF/microwave microstrip antennas are important. Ultrawideband (UWB) wireless communication is a breakthrough technology that opens up new possibilities in today's wireless communication system because of its unique characteristics, which include low cost, high data rate, compact physical size, and low power consumption [1]. The unique characteristics of Vivaldi tapered slot antenna (VTSA) in terms of the end-fire symmetrical radiation pattern, wide bandwidth (BW), simple basic structure, low profile, lightweight and inexpensive manufacture make it preferable in most UWB technology applications such as mm-wave imaging [2], microwave imaging (MI) [3–5], ice-sounding radar [4], ground penetrating radar [6], moist estimation in masonry walls [7], near-field measurement system [8] vehicular communication [9], and unmanned aerial vehicles (UAV) remote sensing [10].

Researchers have tried to reduce the TSA size using many techniques to comply with current industrial standards, such as easy integration with other circuits, low cost, and lower power consumption [11]. A comprehensive review discussing these techniques can be found in [12]. Methods for compactness may include etching slots in the radiation patches' edges [4, 7, 13], corrugations [3, 14–16], loading short pins and resistors [17], parametric studies optimization [18–21] and modifying the antenna structure [22]. A new theory, based on nonuniform called exponential or Vivaldi non-uniform slot profile antenna (ENSPA) or (VNSPA) theory has been proposed [23] to simply reduce the size of UWB VTSA in [19] by 51.94% with enhanced performance. Based on this theory, we demonstrated in this work how the shape of the antenna's exponential nonuniform slot profile (ENSP) can be controlled to achieve 50% and 60% size reductions as compared to the length of the exponential tapered slot profile (ETSP) in [19] without degrading the main performance of the resulting Vivaldi antenna. Based on these reductions and further parametric studies, 72.74 % (Antenna A) and 81.8 % (Antenna B) circuit area reductions are achieved when compared to the UWB VTSA suggested in [19].

Both antennas are designed to work at UWB (3.1–10.6 GHz) with center frequency, fc = 6.85 GHz, and the selected substrate is Rogers RO4003C with $\varepsilon_r = 3.55$, height (h) = 0.813 mm and copper thickness = 0.035 mm. Computer simulation technology (CST) software, which is based on the finite integration technique (FIT), is used to simulate the antennas. It should be noted that when modeling these small antennas, the effect of SMA is considered to achieve closed-measured results.

Breast cancer is one of the leading causes of cancer-related deaths among women worldwide. Early detection significantly improves treatment outcomes and survival rates. Traditional imaging techniques like mammography have limitations, including discomfort, radiation exposure, and reduced sensitivity in dense breast tissues. UWB MI presents a non-invasive, safe, and cost-effective alternative that addresses these limitations by utilizing non-ionizing electromagnetic waves [24]. UWB antennas transmit short pulses of microwave signals into the breast tissue. These signals are scattered by different tissue types based on their dielectric properties. Cancerous tissues have different dielectric properties than healthy tissues and cause distinctive scattering patterns. The received signals are processed to create detailed images of the breast's internal structures, highlighting potential tumors [25–27]. This requires precise detection of the reflected signals utilizing an antenna with higher gain, highly directional radiation patterns, low reflection coefficients, high fidelity of the received signals, and stable group delay. Although for BCD applications, arrays can be more complex and expensive to design and implement than a single antenna, they offer greater efficiency in achieving high detection accuracy. This is because they provide more detailed information, such as improved spatial resolution, an enhanced signal-to-noise ratio, and better penetration and coverage. Additionally, arrays that utilize low-power microwave signals are generally non-invasive and safe for repeated use, making them a suitable option for regular breast cancer screening [28].

Many antennas are proposed for BCD. Several patch antennas have been proposed for BCD, including a rectangular-shaped patch antenna operating at 4.3–4.8 GHz [29], a circular-edged patch antenna covering the 2.26–13.71 GHz range [30], a dual-polarized UWB circular-shaped patch antenna working from 3.9–19 GHz [31], a printed log-periodic shaped patch antenna designed for the 2–5 GHz range [32], and a trapezoidal-shaped patch antenna operating in the 4.2–8.3 GHz and 2.85–9.87 GHz frequency bands [33]. These antennas are fed by a coplanar waveguide (CPW) to achieve a wider bandwidth (BW). In [29, 30], the detection was only based on the difference between scattering parameters of breast phantom (with and without tumor) without reconstructing 2D or 3D images using the MI approach. However, in [33], machine learning algorithms (MLAs) were employed to distinguish between malignant tumors and benign breast tissues. In [31] and [32], noise cluttering is reduced, and antenna performance is enhanced in terms of gain and radiation patterns through the use of dual polarization (horizontal and vertical) and the addition of six epsilon-negative (ENG) metamaterials (MTMs), respectively. However, their 2D images are reconstructed using the Delay-and-Sum (DAS) and Delay multiply-and-sum (DMAS) algorithms, respectively. In [34], a novel compact UWB patch antenna (3.51–18.58 GHz) with a semicircular defected ground structure (SC-DGS) and tapered feed structure is proposed for BCD applications. Although the authors considered Specific Absorption Rate (SAR) calculations and phantom fabrication, no images were reconstructed using the MI approach. 'C' shaped elliptically polarized dielectric resonator Antenna (DRA) is proposed in [35] for BCD where the 2D images are reconstructed using DAS, improved delay and sum (IDAS), and DMAS algorithms with best results obtained using DMAS. In [36] and [37], MTMs and sinusoidal corrugations, are added to the aperture and edges of the proposed (4.8–5 GHz) and (1.1–10 GHz) Antipodal Vivaldi Antennas (AVAs), respectively to improve their detection performance for breast cancer. The detection in [36] was based on the difference between S-parameters. However, MATLAB-based iterative DAS (it-DAS)) algorithm is used in [37] to reconstruct the 2D or 3D images. MTMs and rectangular slotted patches with four star-shaped parasitic components are used to enhance the far field performance (gain and radiation patterns) of UWB (2.0–10.45 GHz) VTSA [3] and (3.8–10.1 GHz) TSA [38] proposed for BCD. MATLAB-based Microwave Radar Based Imaging Toolbox (MERIT) to reconstruct the 3D image is used to reconstruct the 3D image. Recently in [25], two arrays based on the designed VTSA [19] and

VNSA [23] integrated with unequal split nonuniform transmission lines Wilkinson power divider (NTL WPD) [39] are used for BCD. Both arrays provide low SAR value, enhanced BW, and higher gain used successfully to detect breast cancers with different sizes at different locations based on the Robust Time Reverse (RTR) algorithm [40].

In this work, for improved patient comfort and accuracy, ultra-compact VNSAs are proposed, featuring size reductions of 72.74% (Antenna A) and 81.8% (Antenna B) compared to the design proposed in [23] , and employing the RTR algorithm for BCD. Table 1 provides a comprehensive performance comparison of several recent state-of-the-art UWB antennas used for BCD. This comparison includes critical parameters such as substrate, antenna type, BW, maximum gain (MG), phantom fabrication (PhF), the number of antennas used for MI, the number of tumors, MI methods, and SAR considerations.

The proposed antenna is the smallest among the compared options, which directly impacts its feasibility for practical applications in medical imaging. This miniaturization enhances patient comfort during scans. Also, it exhibits a wider bandwidth than those documented in studies [3, 25, 29, 32, 33, 35, 36, 38]. The significance of this bandwidth lies in its ability to improve resolution in imaging, allowing for clearer differentiation between healthy tissue and tumors. This characteristic could lead to earlier detection of malignancies, which is crucial in breast cancer diagnostics.

Moreover, the proposed antenna demonstrates a higher gain compared to antennas in [29, 30, 32–36]. This increased gain contributes to enhanced signal-to-noise ratios, which is essential for accurate tumor detection. The improvement in gain can help mitigate the effects of background noise and artifacts commonly encountered in microwave imaging. Furthermore, the proposed antenna achieves better 2D image reconstruction using the RTR algorithm. This algorithm not only enhances detection accuracy but also significantly reduces background effects such as clutter and side-lobe coupling. Moreover, the proposed antenna provides improved 2D image reconstruction through the use of the RTR algorithm, which boosts detection accuracy by efficiently minimizing background interference, including clutter and side-lobe coupling. A detailed explanation of how the RTR algorithm operates and its specific advantages in imaging quality is provided in section 4, emphasizing its role in enhancing the delineation of tumor boundaries and improving the reliability of tumor identification.

1.1. Contribution of the study

This study addresses critical limitations in using UWB antennas for MI in breast cancer detection. It introduces an innovative design of ultra-compact Vivaldi antennas based on the Vivaldi Non-Uniform Slot Profile Antenna (VNSPA) theory. In addition, the proposed antenna offers enhanced compactness by substantial reductions in slot length (50% and 60%) and circuit area (72.74% for Antenna A and 81.8% for Antenna B), making them significantly more compact than traditional UWB antennas. This compactness enhances patient comfort during imaging procedures and facilitates easier integration into medical devices. Antenna A and Antenna B demonstrate impressive performance, matching S_{11} values below −11.36 dB and −10.21 dB, and peak gains of 5.9 dBi and 6 dBi, respectively. These metrics ensure better signal quality and reliability over a broad frequency range (2.63–12.33 GHz for Antenna A and 3.16–14.34 GHz for Antenna B). Despite being 30.58% smaller than Antenna A, Antenna B offers a 13.24% increase in bandwidth and a 1.7% gain enhancement. This highlights the effectiveness of the ENSP shape in optimizing antenna performance, thus providing higher resolution and better penetration in imaging applications. Effective Tumor Detection: Simulations and practical tests using CST software confirm that the proposed antennas can detect tumors in the breast with high accuracy. This is evidenced by the directive stable radiation patterns and low SAR values, which are crucial for safe and effective medical imaging.

The following sections 2 and 3, present the design and analysis of the proposed antennas using VNSPA theory and compare the optimized simulation findings with the hardware measurements to evaluate the proposed antennas, respectively. Section 4 explains a simulation and measurement scenario BCD for Antenna B. Finally, section 5 concludes the work.

2. Antenna design and analysis

Significant efforts are required to reduce its size while maintaining an acceptable performance to facilitate the antenna integration with other circuitry and satisfy user demands. In this work, the ENSPA or VNSPA theory recently developed by Saleh *et al* in [23] is exploited to design an ultra-compact UWB Vivaldi antenna with enhanced performance. The new aspect of this study is obtaining more compactness from different suitable ENSP shapes without compromising the performance of the final Vivaldi antenna. The Vivaldi antenna and the optimized shapes are selected to achieve higher directive gain. This can be achieved by controlling constraints in the optimization MATLAB code. According to VNSPA theory, ENSP and ETSP will be equivalent if their ABCD

Table 1. UWB antennas used in the literature for BCD (2020–2024).

References	ε_r/h (mm)	Antenna type	BW (GHz)	MG (dBi)	Size $\lambda_0 \times \lambda_0$	PhF	No of antennas	No of tumors	MI methods	SAR
[34]	4.3/1.6	patch	3.51–18.58	5.86	0.19 × 0.26	Yes	1	1	NU	Yes
[25]	3.5/0.813	VNSA	3.24–11.1	8.14	0.95 × 0.48	No	2	1,2,3	RTR	Yes
[38]	2.2/1.575	TSA	3.8–10.1	6	0.3 × 0.28	Yes	2	1	MERIT	No
[33]	1.9/0.17	patch	2.85–9.87	3.5	0.23 × 0.43	Yes	1	1	NU	Yes
[30]	2.2/0.254	patch	2.26–13.71	3.84	0.19 × 0.28	No	1,2	1	NU	Yes
[29]	10.2/0.64	patch	4.3–4.8	2	0.37 × 0.43	Yes	1, 2	1	NU	No
[31]	3.5/0.2	patch	3.9–19	NA	0.39 × 0.39	Yes	8	1,2	DAS	No
[32]	4.4/1.6	patch	1.75–5	5.5	0.29 × 0.23	No	16	1,2	DAS & DAMAS	No
[35]	4.4,9.8/1.57,4	DRA	3.6–11.2	3.84	0.48 × 0.48	YES	1	1	DAS & DAMAS	No
[36]	10.2/0.64	AVA	6.17–8	5.8	1.38 × 0.95	Yes	8	1	NU	No
[3]	2.2/1.575	VTSA	2–11.79	7.9	0.48 × 0.42	Yes	9	1	MERIT	Yes
This work	3.5/0.813	VNSA	3.16–14.34	6	0.2 × 0.13	Yes	9	1,2	RTR	Yes

*NU: not used, NA: not available, and λ_0 is the free space wavelength at the lower frequency.

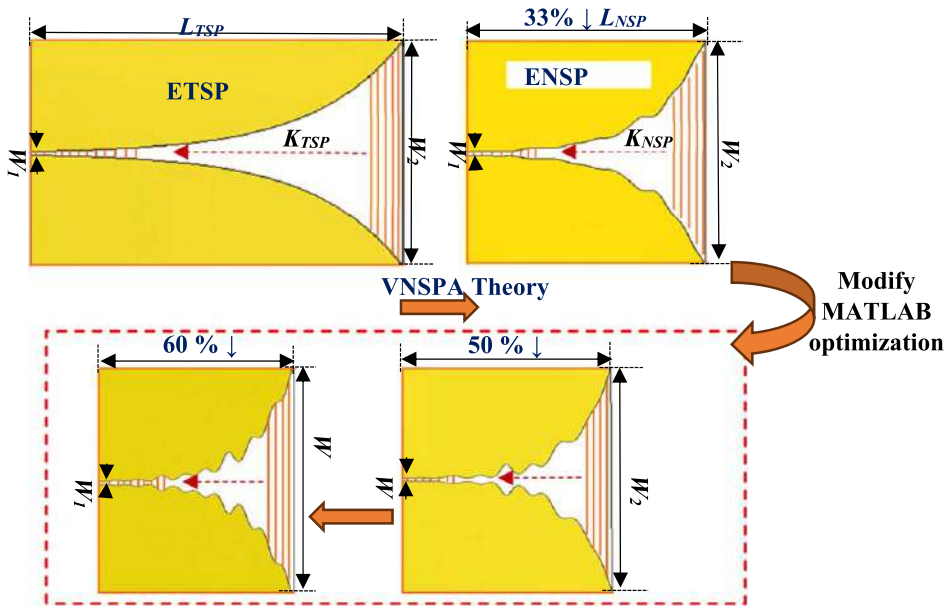

Figure 1. Development of the new ENSP profiles based on VNSPA theory [23].

parameters are identical at the targeted frequency range. The ABCD parameters can be subdivided into uniform slots (K_{TSP} and K_{NSP}), as shown in figure 1.

ETSP is defined by [41] as follows

$$W_{TSP}(x) = \pm \mathrm{A}\ \mathrm{e}^{ra * \mathrm{x}} \tag{1}$$

where A is half the opening of the antenna aperture (W_1), *ra* is the taper rate and x is the position along L_{TSP}.

However, ENSP can be defined using truncated Fourier series as follows:

$$\ln\left(W_{NSP}(x)/W_{TSP}(x)\right) = \sum_{n=0}^{\mathrm{N}} C_n \cos\left(\frac{2\pi n x}{L_{NSP}}\right) \tag{2}$$

where N = 10 [42] and C_n is the Fourier series coefficients that can be optimized using the built-in MATLAB function, fmincon which is used to find the minimum of constrained nonlinear multivariable function [43]. The total *ABCD* matrix of these nonuniform profiles (ETSP and ENSP) will be :

$$\begin{bmatrix} A & B \\ C & D \end{bmatrix} = \prod_{i=1}^{K} \begin{bmatrix} A_K & B_K \\ C_K & D_K \end{bmatrix} \tag{3}$$

where

$$A_i = D_i = \cos(\Delta\theta), \tag{3.1}$$

$$B_i = j\,Z(x)((i\ -\ 0.5)\Delta x)\cos(\Delta\theta), \tag{3.2}$$

$$C_I = \frac{\mathrm{jsin}(\Delta\theta)}{Z(\mathrm{x})((i-0.5)\Delta x)},\ i = 1,\ 2,\ldots.K,\ \Delta x = \frac{L}{K} \tag{3.3}$$

L and K are the length and subdivisions of ENSP (L_{NSP} and K_{NSP}) or ETSP (L_{TSP} and K_{TSP}), respectivelyand

$$\Delta\theta_N = \frac{2\pi}{\lambda}\Delta x = \frac{2\pi f}{C}\sqrt{\varepsilon_{eff_s}}\ \Delta x \tag{3.4}$$

$\varepsilon_{eff_s} = \frac{\varepsilon_r + 1}{2}$is the effective dielectric constant of the slot line.

To define the characteristics impedance of the slot line, an empirical formula based on the slot line width (W) in [44] can be found.

The optimum values of C_ns are based on reducing the difference between the ETSP and ENSP *ABCD* parameters within the required band (UWB), where the error function can be defined as:

$$\mathrm{Error} = \sqrt{\frac{1}{M}\sum_{m=1}^{M}\frac{1}{4}(|A_{Nsp} - A_{TSP}|^2 + Z(x)_{TSP}^{-2}|B_{NSP} - B_{TSP}|^2 + Z(x)_{TSP}^{2}|C_{NSP} - C_{TSP}|^2 + |D_{NSP} - D_{TSP}|^2)} \tag{4}$$

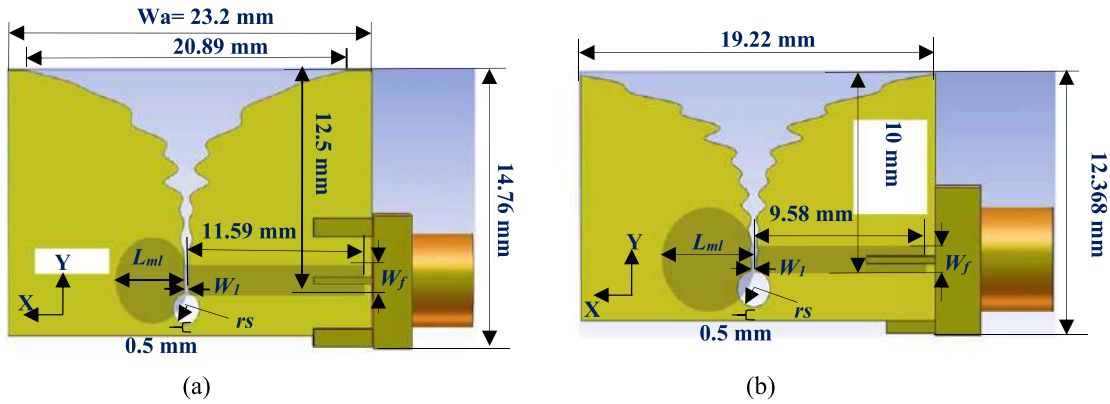

Figure 2. Layouts of the proposed compact UWB (a) Antenna A and (b) Antenna B.

Table 2. Optimized C_{ns} for ENSP at $\Delta f = 0.025$ GHz and $KNSP = KTSP = 50$.

Error = 0.0071										
C_0	C_1	C_2	C_3	C_4	C_5	C_6	C_7	C_8	C_9	C_{10}
0.1549	−0.0908	−0.0204	−0.0145	0.0156	0.0272	−0.0506	0.0430	0.0473	−0.1185	0.0138

Table 3. Optimized C_ns for ENSP at $\Delta f = 0.0125$ GHz and $K_{NSP} = K_{TSP} = 100$.

Error = 0.0498										
C_0	C_1	C_2	C_3	C_4	C_5	C_6	C_7	C_8	C_9	C_{10}
0.2060	−0.1272	−0.0204	0.0304	−0.0933	0.0231	0.0013	0.0747	−0.1146	0.0529	−0.0256

where M is the number of the frequencies f_m ($m = 1, 2, \ldots M$) with frequency increment Δf at the UWB frequency band. A_{TSP}, B_{TSP}, $C_{TSP,}$ and D_{TSP} are the $ABCD$ matrix parameters of ETSP, and A_{NSP}, B_{NSP}, $C_{NSP,}$ and D_{NSP} are the $ABCD$ matrix parameters of ENSP.

To ensure that the resultant antenna's performance is not compromised, the aperture opening (W_1) and width (W_2) of the resulting ENSP and ETSP should be equal, and the nonuniform width shouldn't exceed these values (i.e., $W_1 < W_N(x) < W_2$) to achieve acceptable profile. Using this concept and the modified MATLAB optimization code with different K_{TSP}, $K_{NSP,}$ and frequency increment Δf at the UWB frequency band within the required constraints, length reductions of 50% and 60% were obtained for two different ENSP shapes, which are 20% and 30% smaller than the one achieved in [19]. After numerous trials of executing the MATLAB code, the optimal C_n depicted in tables 2 and 3 is chosen to draw the profiles displayed in the dashed rectangle of figure 1 with 50% and 60%. The main optimization MATLAB code is explained in the appendix.

2.1. Parametric studies

For the 50% and 60 % compactness, i.e., $L_{NSP} = (1–0.5) \times L_{TSP}$, and $L_{NSP} = (1–0.6) \times L_{TSP}$, the final layouts of Antenna A and B with 72.74 % and 81.1 % circuit area reductions are illustrated in figures 2(a) and 2(b), respectively. These optimum dimensions are achieved using parametric studies based on CST simulation on the quarter-wavelength microstrip line (L_{ml}), the circular slot's radius(rs), $rem = W_a$ (antenna width)-L_{ml}, and the width of the microstrip feed line (W_f) for Antenna A and B as depicted in figures 3(a)–(d), and 3(a)–(d), respectively.

L_{ml} at the microstrip to slot (M/S) transition affects the BW and matching, where the BW enhances as L_{ml} decreases, as shown in figure 3(a). However, not all the values satisfy the required matching, such as $L_{ml} = 3.9$ mm ($S_{11} < -6.79$ dB at 2.8–12.95 GHz and MG = 6.1 dBi). $L_{ml} = 4.8$ mm ($S_{11} < -11.2$ dB at 2.78–12.51 GHz and MG = 6 dBi) is selected due to its 6.47% wider BW than the optimized value of VTSA at $L_{ml} = 5.7$ mm ($S_{11} < -11.24$ dB at 2.82–11.92 GHz and MG = 6 dBi)) and 17.27% wider BW and better S_{11}than at $L_{ml} = 6.6$ mm ($S_{11} < -10.83$ dB at 2.82–10.87 GHz and MG = 5.8 dBi). rs directly affects the matching where the best result is obtained at $rs = 0.88$ mm, as illustrated in figure 3(b). Figure 3(c) shows that the best matching and gain is obtained at $rem = 18.4$ mm ($S_{11} < -11.2$ dB at 2.78–12.51 GHz with MG = 6 dBi), which is better

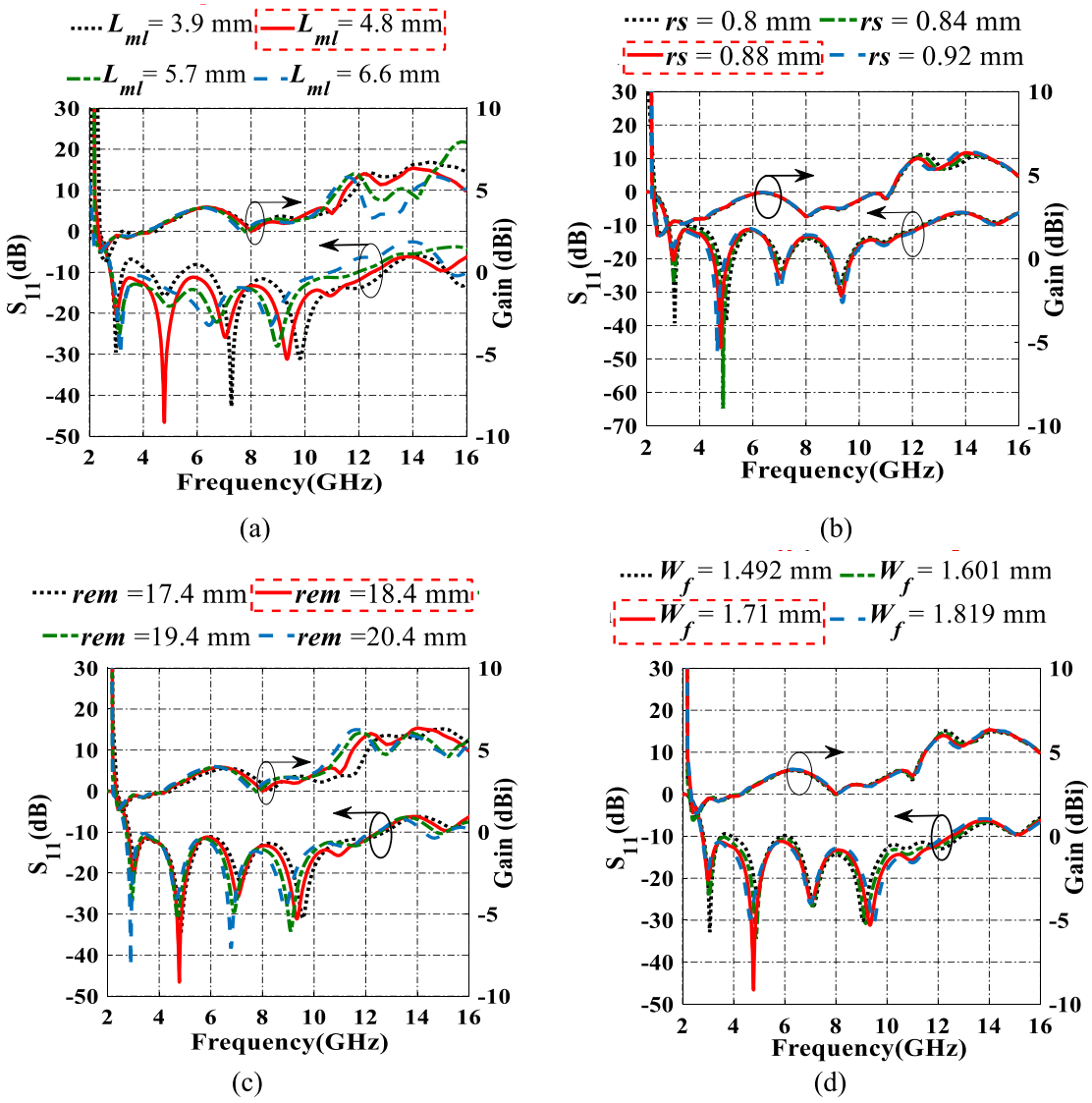

Figure 3. S_{11} and gain parametric study of the proposed compact UWB Antenna A on (a) L_{mb} (b) *rs*, (c) *rem*, and (d) W_f.

than that at *rem* = 17.4 mm (S_{11} < −10.85 dB at 2.92–13.34 GHz with MG = 5.92 dBi). Although the gain at *rem* = 19.4 mm (S_{11} <−10.33 dB, at 2.78–12.51 GHz with MG = 6.05 dBi) and *rem* = 20.4 mm (S_{11} < −10.33 dB at 2.74–12.51 GHz and MG = 6.24 dBi) are 0.83% and 3.84%, respectively higher than that at *rem* = 18.4 mm, it is selected due to its better matching (S_{11}<−11.2 dB), and smaller length. Figure 3(d) shows that the matching with W_f<1.71 mm worsens. However, with W_f= 1.71 mm (S_{11} < −11.2 dB) at 2.78–12.51 GHz and MG = 6 dBi) this design is selected due to its 2.57 % wider BW and 3.67 % higher gain than the calculated one, W_f= 1.819 mm (S_{11} <−11.2 dB at 2.78–12.26 GHz and MG = 5.78 dBi).

Figure 4(a) shows that although the 12 % wider BW provided by L_{ml} = 4.74 mm (S_{11} < −9.61 dB at 2.4–15.27 GHz and MG = 6 dBi), L_{ml} = 5.22 mm (S_{11} < −10.2 dB at 3.4–14.724 GHz and MG = 6.15 dBi) is selected due its better matching. The matching is improved as *rs* and *rem* increase. However, as depicted in figure 4(b), the best value is obtained at *rs* = 0.934 mm (S_{11} <−10.2 dB at 3.4–14.724 GHz and MG = 6.15 dBi), which is better than *rs* = 1.034 mm (S_{11} < −9.05 dB at 3.4–14.724 GHz and peak gain = 5.96 dBi) in terms of matching and gain. Figure 4(c) depicts that as *rem* decreases, the BW enhances for *rem* = 12 mm (S_{11} < −9.07 dB at 3.63–15.45 GHz and MG = 4.84 dBi) and *rem* = 13 mm (S_{11} <−9.42 dB at 3.51–15.09 GHz and MG = 5.38 dBi). However, the design with *rem* = 14 mm (S_{11} < −10.2 dB at 3.4–14.724 GHz and MG = 6.15 dBi) is selected due to its better matching and gain. Although the gain provided by *rem* = 15 mm (S_{11} < −10.13 dB at 3.3–14.37 GHz and MG = 6.2 dBi) is 0.81 % higher than that at *rem* = 14 mm, it is not selected to avoid the larger size. Finally, figure 4(d) illustrates that W_f= 1.362 mm (S_{11} < −10.2 dB at 3.4–14.724 GHz and MG = 6.15 dBi) provides the best matching to a 50 Ω SMA connector. Based on these optimized parameters, the fabricated prototypes of Antenna A and B are shown in figures 5(a) and (b), respectively.

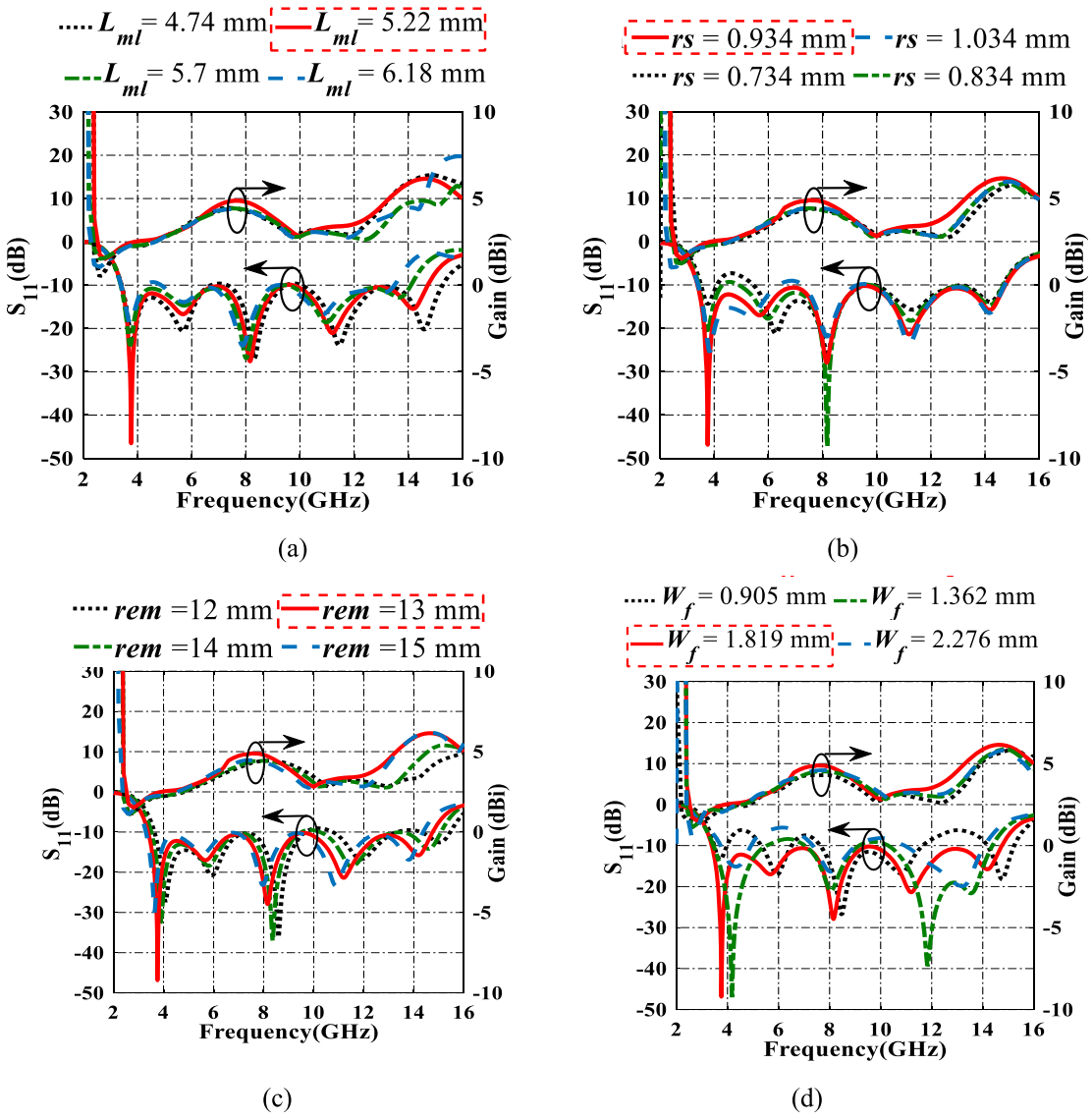

Figure 4. S_{11} and gain parametric study of the proposed compact UWB Antenna B on (a) L_{ml}, (b) *rs*, (c) *rem*, and (d) W_f.

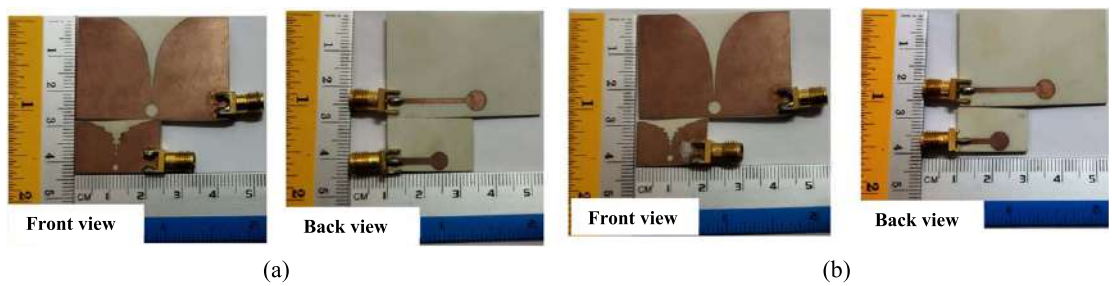

Figure 5. Photograph of the fabricated compact UWB (a) Antenna A and (b) Antenna B in comparison to VTSA in [19].

As illustrated in table 4 by comparing the simulated results of Antenna A and B to VTSA [19], it should be noted that although their size is reduced by 72.74 % and 81.1 %, respectively, they provide good impedance matching with enhanced BW and moderate peak gain. Moreover, the 14.1 % BW and 2.44 % gain improvements of Antenna B, despite its 30.58 % size reduction as compared to Antenna A, demonstrates the effectiveness of ENSPA theory and the significance of the MATLAB optimization code to obtain the appropriate ENSP shape for designing ultra- compact antenna with high-performance.

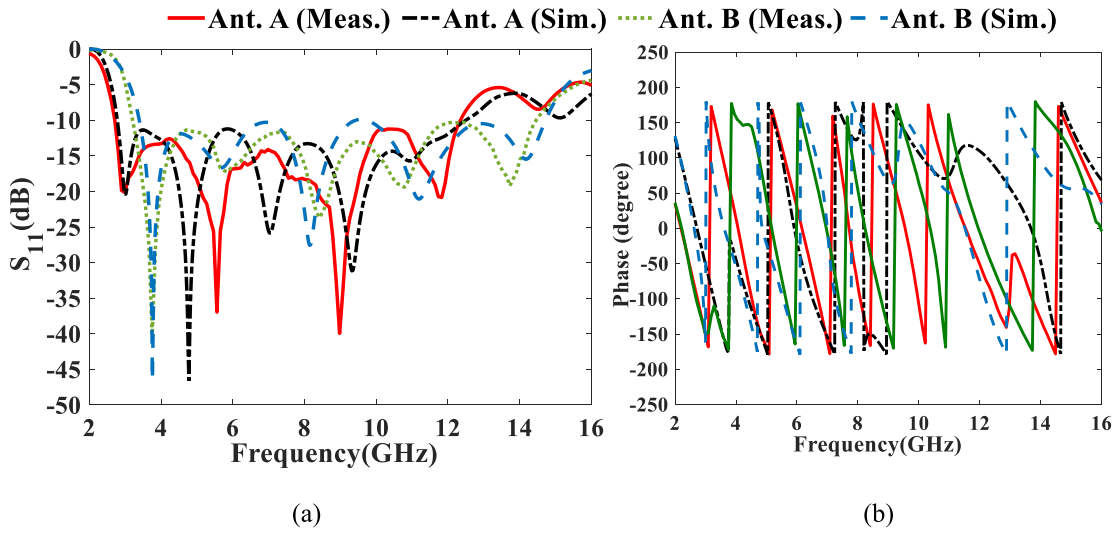

Figure 6. Simulated and measured (a) S_{11} and (b) phase of the proposed compact UWB Ant. A and B.

Table 4. The simulated results of proposed antennas compared to VTSA in [19].

Type	S_{11}(dB)	MG	Size: mm^2
Antenna A	<-11.2 at 2.78–12.51 GHz	6 dBi	23.2×14.76
Antenna B	<-10.2 at 3.4–14.724 GHz	6.15 dBi	19.22×12.368
VTSA [19]	<-10.84 at 2.97–12.71 GHz	6.63 dBi	29.28×42.9

3. Results and discussions

The smaller antenna size obtained by applying the VNSPA theory has not degraded the performance in terms of BW and gain of the proposed UWB antennas when compared to VTSA [19]. This demonstrates the effectiveness of controlling the ENSP shape to get the required compactness while maintaining the main performance of the resulting antenna.

In figure 6(a), the antennas exhibit good matching, indicated by their low reflection coefficients ($S_{11} < -11.36$ dB for Antenna A (Ant. A) and $S_{11} < -10.21$ dB for Antenna B (Ant. B)), across a wide BW. This low S_{11} indicates that a minimal portion of the input signal is reflected back, thus ensuring that a significant amount of power is effectively transmitted through the antennas. This characteristic is crucial for wideband antennas, particularly in applications such as UWB microwave imaging, where efficiency and broad frequency operation are essential. Both antennas maintain strong performance across wide frequency ranges—Ant. A from 2.63 to 12.33 GHz and Ant. B from 3.16 to 14.34 GHz. Notably, Ant. B, although 30.58% smaller in size, provides a 13.24% improvement in BW, demonstrating the effectiveness of its optimized ENSP shape. This improvement is achieved through MATLAB optimization, which fine-tunes the antenna's geometry to enhance BW while maintaining compactness. The slight phase shift observed in figure 6(b) is likely due to the differing lengths of the ENSP for both antennas. Phase shifts indicate variations in the timing of the electromagnetic waves emitted by the antennas, which can influence their signal propagation and reception characteristics. Such shifts can arise from changes in physical dimensions and configurations, affecting how the antennas respond to incoming signals. Despite this phase difference, both antennas maintain efficient operation within their intended frequency bands, demonstrating that effective design and optimization techniques can mitigate potential adverse effects from size reductions and geometric alterations.

The good matching results for both antennas can be explained with the simulated input impedance depicted in figure 7. The impedance characteristics reveal that the real part of the impedance oscillates around 50 Ω, while the imaginary part approaches 0 Ω. This oscillation indicates that the antennas are effectively matched to the characteristic impedance of the transmission line, facilitating maximum power transfer and minimizing signal reflection at the feed point. In RF applications, particularly in UWB antennas, achieving impedance matching is

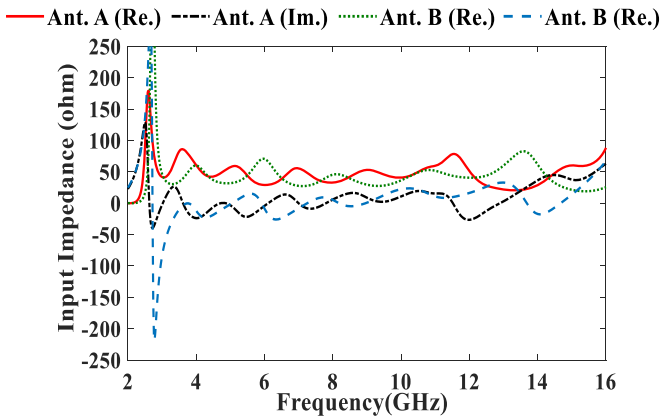

Figure 7. The simulated input impedance of the proposed compact UWB Ant. A and B.

critical as it directly influences the efficiency and performance of the device across its operational bandwidth [41, 45].

The discrepancy between the simulated and measured results arises from measurement and manufacturing errors, including issues like SMA soldering connectors (produce insertion loss), laboratory errors (such as reflections from other devices), and differences between the simulation and measurement environments where the simulation, numerical technique (Finite Integration Technique (FIT) in CST) to approximate the fields within certain boundary conditions. It should be noted that, although there is a discrepancy between the two antennas, they still achieve a reasonable and acceptable matching requirement within the UWB frequency band [46]. Despite the discrepancy in the resonance peaks for Antenna A between the simulated and measured results (figure 6(a)), they still have the same number of peaks with a frequency shift within the required frequency band for the reasons mentioned above.

To explain the difference between the simulated and measured results, a statistical analysis is conducted to understand the variations in the measured results for the proposed antennas, using a sample set of the fabricated antennas (Ant. A and Ant. B) from the same batch. Firstly, the key performance of each antenna (S_{11} and MG) is measured. Then the statistical metrics, including Mean and Standard Deviation (M & SD), Coefficient of Variation (CV), and 95% confidence intervals (95% CI), are calculated. M& SD provides insights into the average performance and variability of the antennas, while CV and CI help to understand the relative variability concerning the mean values and indicate the range within which the true performance metrics are expected to lie, respectively. Finally, the statistical analysis of the measured parameters is summarized below:

1. Ant. A

a. S11: M = −11.36 dB, SD = 0.3 dB, CV = 2.64%, 95% CI = [−11.66, −11.06] dB

b. MG: M = 5.9 dBi, SD = 0.2 dBi, CV = 3.39%, 95% CI = [5.7, 6.1] dBi

2. Ant. B

b. S11: M = −10.21 dB, SD = 0.4 dB, CV = 3.92%, 95% CI = [−10.61, −9.81] dB

c. MG: M = 6 dBi, SD = 0.3 dBi, CV = 5%, 95% CI = [5.7, 6.3] dBi

The statistical analysis shows that the variations in the measured values are within acceptable limits and align with the expected tolerances for production processes. These variations do not significantly affect the overall performance of the antennas in the context of breast cancer detection using UWB microwave imaging.

In UWB applications, achieving acceptable radio signal transmission requires a flat group delay (GD) across the entire frequency spectrum [47]. A flat GD indicates that all frequency components of the signal experience similar delays as they propagate, which is crucial for maintaining signal integrity and reducing distortion in high-speed data communications. As shown in figure 8(a), the CST simulation and measurement setups utilize a face-to-face (F2F) configuration in the E-plane, which allows for direct comparison of the two antenna samples. As depicted in figure 8(b), the approximately flat GD (Meas. 0.5 ns and Sim. 0.25 ns) provided by Antenna B is smaller than Antenna A (Meas. 0.6 ns and Sim. 0.4 ns), where the signal propagates faster, taking the shortest

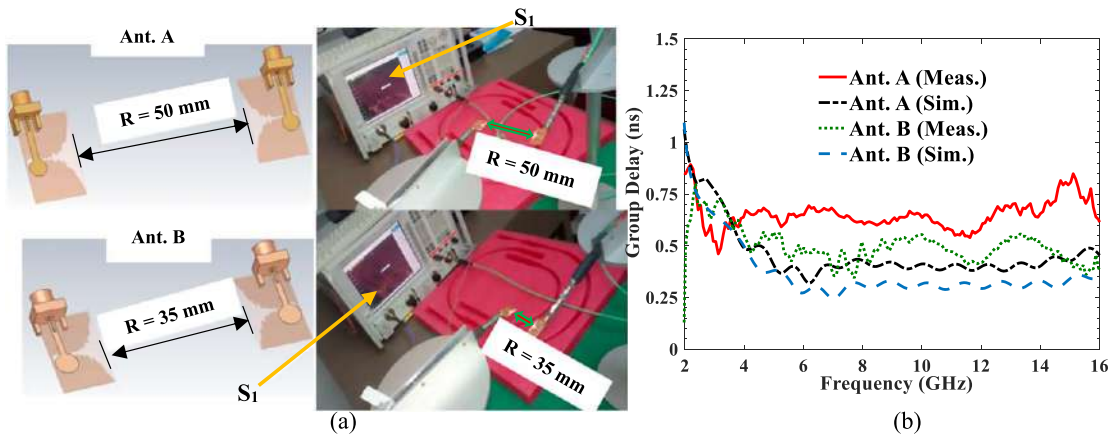

Figure 8. (a) Simulation and measurement of GD setups and (b) Simulated and measured group delay of the proposed compact UWB Ant. A and B.

path. This small flat GD indicates that the proposed antennas are efficient in facilitating signal propagation, allowing signals to traverse the antenna's structure and minimizing the variation in signal timing for different frequency components, which is essential for effective signal transmission in UWB applications. Such characteristics help reduce inter-symbol interference (ISI), thus enhancing the overall performance of the communication system. The ability to maintain a small flat GD across UWB frequencies further underscores the effectiveness of the antenna design in optimizing the propagation characteristics of the transmitted signal.

The radiation patterns of Antenna A and Antenna B, as depicted in figure 9, illustrate that both antennas achieve approximately stable end-fire and dipole radiation patterns for their respective E (XY-plane) and H (XZ-plane) planes. The end-fire pattern signifies that the antenna primarily radiates energy in the direction of its length, which is particularly beneficial for applications requiring focused signal transmission, such as in UWB communication systems. This configuration enhances the antenna's ability to transmit and receive signals effectively, minimizing interference and optimizing the strength of the signal across the desired frequency range. In addition, the dipole radiation pattern indicates that both antennas maintain a well-distributed radiation field, allowing for a consistent performance in various orientations, which is essential for achieving reliable connectivity in real-world scenarios.

The ability of both antennas to maintain stable radiation patterns across the UWB frequency spectrum is critical for ensuring effective communication in diverse applications, such as medical imaging and wireless data transfer. A stable dipole pattern, in particular, ensures that the antennas can efficiently couple with incoming electromagnetic waves, leading to improved gain and directivity. These characteristics enable robust performance in environments with varying signal propagation conditions, making them suitable for advanced applications in wireless technologies. The findings suggest that the design optimizations employed in Antenna A and B effectively balance size, bandwidth, and radiation characteristics, contributing to their overall efficiency and reliability in UWB applications.

The results in figure 10 indicate that both Antenna A and Antenna B achieve commendable moderate peak gains of 5.9 dBi and 6 dBi, respectively, despite their compact sizes facilitated by the VNSPA theory. This performance underscores the efficiency of the VNSPA approach in reducing the physical dimensions of Vivaldi antennas without compromising their performance. The increase in peak gain of 1.7% for Antenna B compared to Antenna A highlights the significant impact of the optimization constraints applied in the MATLAB code, which played a critical role in getting the acceptable ENSP shape to maintain effective radiation characteristics [23]. This improvement is essential in microwave medical imaging applications, particularly for cancer detection, where efficient signal transmission and reception are vital for accurate imaging.

Moreover, the total radiation efficiency of both antennas, measured between 82.27% and 96.9% for Antenna A and between 71.48% and 96.86% for Antenna B, demonstrates robust performance within the UWB frequency range of 2.63–12.33 GHz for Antenna A and 3.16–14.34 GHz for Antenna B. High radiation efficiency is crucial in medical imaging applications as it ensures that a significant amount of the radiated energy is effectively utilized in imaging the target tissues, leading to improved image quality and diagnostic accuracy. In the context of cancer detection, this translates into better identification of tumor characteristics, enhancing the overall efficacy of microwave imaging techniques in clinical settings. Thus, the findings reinforce the importance of utilizing advanced antenna design theories to optimize performance while ensuring compactness, making them suitable for non-invasive medical imaging technologies.

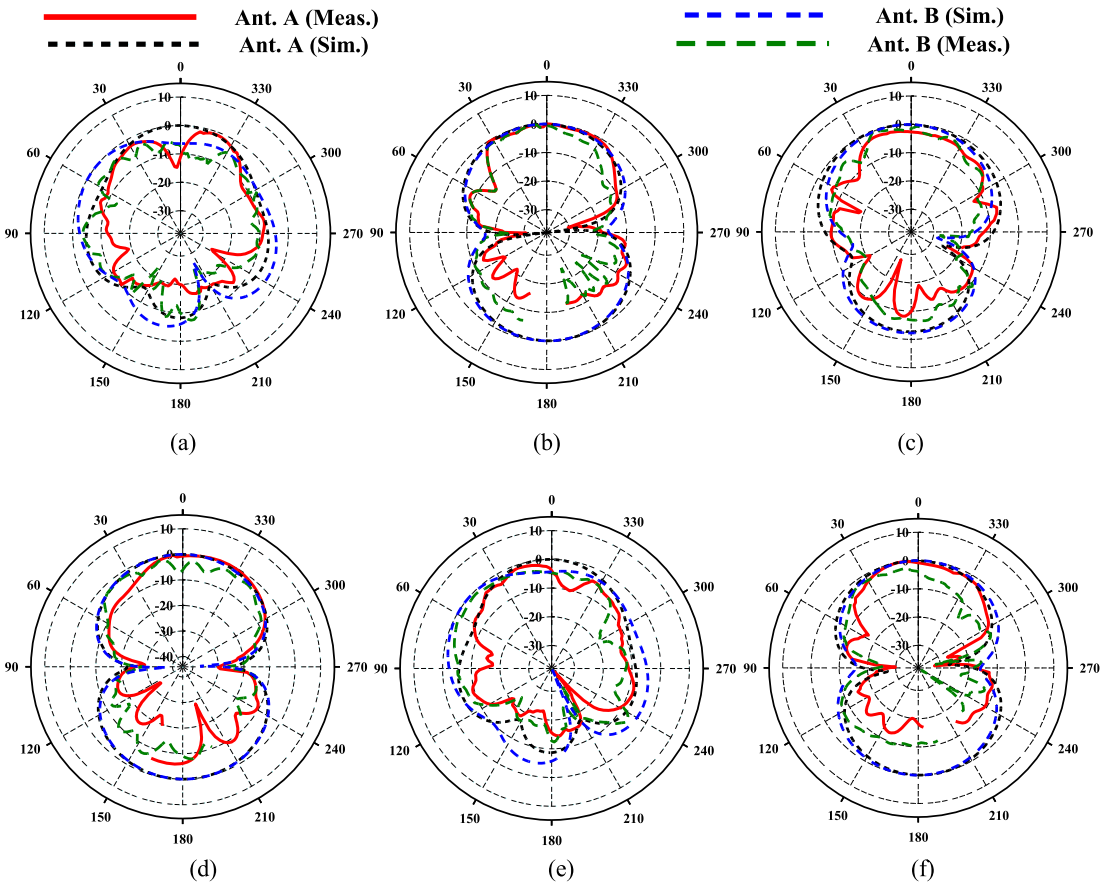

Figure 9. Simulated and measured radiation pattern of the proposed compact UWB Antenna A and B at 5.84 GHz (a) E and(b) H, 8.65 GHz (c) E and (d) H, 10 GHz (e) E and(f) H.

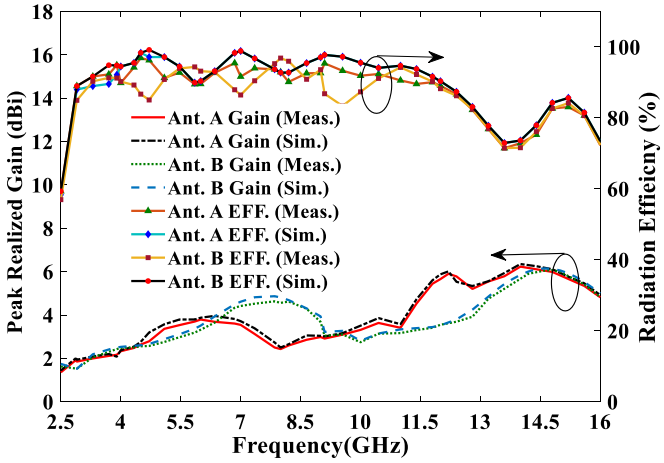

Figure 10. Simulated and measured peak realized gain with the total efficiency of the proposed compact UWB Ant. A and B.

The discrepancy in radiation patterns, gain, and efficiency between the simulated and measured findings is attributable to manufacturing tolerance, improper soldering of SMA connectors, cable loss of the antenna feeder, and the difference between the simulation and actual measurement conditions.

Table 5 presents a comprehensive comparison between the proposed UWB compact Antennas A and B and the latest related work in the literature over the past seven years. It can be noted that the proposed antennas are the smallest with wider BW among the recent studies evaluated. This significant reduction in size is particularly advantageous in medical applications where compact designs enhance patient comfort and facilitate integration into existing imaging systems.

Table 5. Other related TSAs at different wide and ultra-wide frequency bands for the last seven years in the literature.

References	ε_r	S_{11}(dB) at Freq. Band, BW(GHz)	Gain (dBi)	Compactness (C) & PE techniques	Volume: mm^3
Ant. A	3.55	<−11.36 at 2.63–12.33, 9.7	2–5.9	C & PE: VNSPA theory	23.2 × 14.76 × 0.813
Ant. B	3.55	<−10.21 at 3.16–14.34, 11.18	1.9–6	C & PE: VNSPA theory	19.22 × 12.368 × 0.813
[3]	2.2	< −11.14 at 2–11.79, 9.79	0–7.9	C: Side slots and PE: Metamaterials	40 × 46 × 1.575
[20]	4.4	<−10.33 at 2—>8, >6	7.2–8.7	C: Parametric studies & PE: Corrugations & directors	110 × 96 × 0.8
[5]	4.3	<−14 at 3–3.9,0.9 & <−11.42 at 3.9–10.4, 6.5	3–9.5	C: Hemi cylindrical slots at the edges & PE: directors	49 × 48.5 × 0.8
[7]	4.4	<−10.55 at 1.55—>10, >8.45	NA	C: rectangular slots at the edges	75 × 130 × 1.4
[13]	4.4	<10.2 at 2.83–11.31, 8.48	3.2–7.5	C: hooked slots & PE: director & metamaterials	32 × 30 × 0.8
[16]	4.3	< −10.4 at 1.1–8, 6.9	4.9–10	C: Corrugations and PE: director	82 × 55 × 1.6
[19]	3.55	<−11.15 at 3.14–13.48, 10.34	2.2–6.51	C & PE: Parametric studies	42.9 × 29.28 × 0.813
[21]	5.2	<−10 at 2.96–5.05, 2.09/ 5.58–8.52, 2.94	0–6.57	C: Parametric studies & PE: embedded patch at the edge	45 × 40 × 0.8
[23]	3.55	<−10.89 at 2.9–13.55,10.65	1.8–6.91	C & PE: VNSPA theory	29.8 × 20.26 × 0.813

Despite the substantial size reductions, both antennas maintain good matching characteristics, which are essential for efficient energy transfer and overall performance. Good matching ensures that the antennas can effectively transmit and receive signals without significant loss, thereby improving the overall efficiency of the system. While the proposed antennas achieve moderate gain, it is worth noting that higher gain levels, as seen in [3, 5, 13, 16, 20, 21], are attributed to the larger physical size of the antennas in those studies. The balance between size and gain in the proposed designs is a significant advantage, as the antennas achieve compactness without sacrificing too much performance. This trade-off between maintaining a smaller footprint and preserving effective gain highlights the innovative approach of the design, ensuring that the antennas remain suitable for practical medical applications where space constraints are often a critical factor.

By comparing Antennas A and B to recent studies such as those in [19], and [23] , it is evident that the use of VNSPA theory has led to significant size reductions. Antenna A's size has been minimized by 72.74% and 81.8%, while Antenna B has seen reductions of 42.51% and 60.63%, depending on the specific configuration. Despite these notable size reductions, the corresponding decrease in gain remains minimal—9.4% and 7.83% for Antenna A, and 14.62% and 13.17% for Antenna B. This demonstrates the effectiveness of VNSPA theory in optimizing antenna dimensions while maintaining performance, striking a fine balance between compactness and gain retention, which is essential for clinical applications that require reliable imaging results.

A notable feature of this design is its simplicity in achieving size reduction without the need for performance-enhancing (PE) techniques often used in other studies [3, 5, 13, 16, 20, 21] such as the inclusion of slots, corrugations metamaterials, directors, or embedded patches. In contrast, the proposed antennas maintain high efficiency through innovative design alone. This highlights that the antennas can deliver excellent performance without the added complexity or potential trade-offs that PE techniques may introduce. The success of these designs in maintaining performance while minimizing size not only underscores the value of the VNSPA theory but also opens up opportunities for future advancements in antenna technology, particularly for medical applications where compactness and efficiency are critical.

4. Breast cancer detection scenario

The MI idea is based on the difference in electrical characteristics of normal and malignant cells (in the human breast, for example), which may be acquired by transmitting UWB signals to the breast (with and without tumor) and recording the backscattered S-parameters. This approach was recently successfully applied in [25] for the UWB VNSA [23] by using four compact arrays fed by 2:1 unequal split nonuniform transmission lines Wilkinson power divider (NTL WPD) [39] . Despite being 30.58% smaller, Antenna B provides a 13.24% superior bandwidth and a 1.7% gain enhancement compared to Antenna A. These advantages make Antenna B the preferred choice for breast cancer detection due to its benefits in patient comfort and ease of integration. Based on the UWB MI approach, nine samples of Antenna B are placed around a hemispherical breast phantom (radius = 50 mm) with and without a tumor (central tumor with a diameter of less than 10 mm). Table 6 illustrates the electric properties and densities of the breast phantom tissues, which can be found in [48, 49] and [50], respectively.

To guarantee the body's safety from harmful electromagnetic radiation, a specific absorption rate (SAR) is calculated using CST for both antennas based on the limit recommended by the Council of the European Union

Table 6. Densities and electric properties of the breast phantom tissues.

Parameters	Skin	Fat	Fibro glandular	Tumor
Mass density (Kg/m^3)	1090	950	1000	440
ε_r	34.2	4.32	39.65	54.9
conductivity(S/m)	4.67	0.509	7.65	4
radius (mm)	100	95	90	5
Thickness(mm)	5	5	—	—

Table 7. Simulated 3D SAR results over 10 g of the proposed Antenna B.

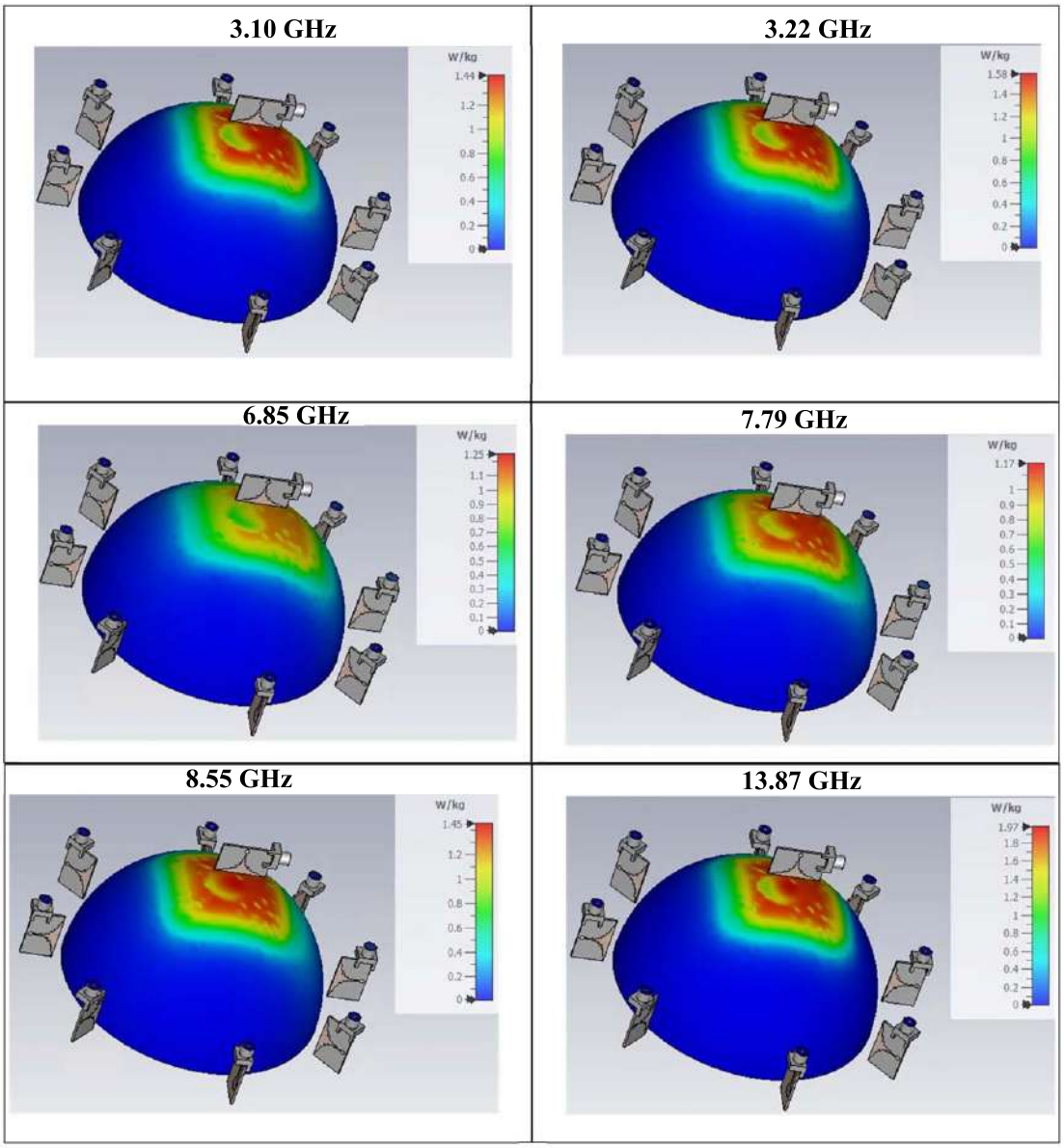

(2 W kg^{-1} averaged over 10 g of actual tissue). For an input power of 100 mW (20 dBm), the SAR results at different resonances of Antenna B are presented in table 7, demonstrating that they do not exceed the safety limit. In addition, there is some space between the antenna, and the breast phantom itself. Therefore, a perfect mutual coupling exists between the antenna and the environment, and the high gain cannot affect the body.

As shown in figures 11(a) and (b), the system utilizes a set of nine compact UWB antennas with the dimensions of 19.22 × 12.368 mm^2, to illuminate the breast tissue and collect scattered electromagnetic (EM)

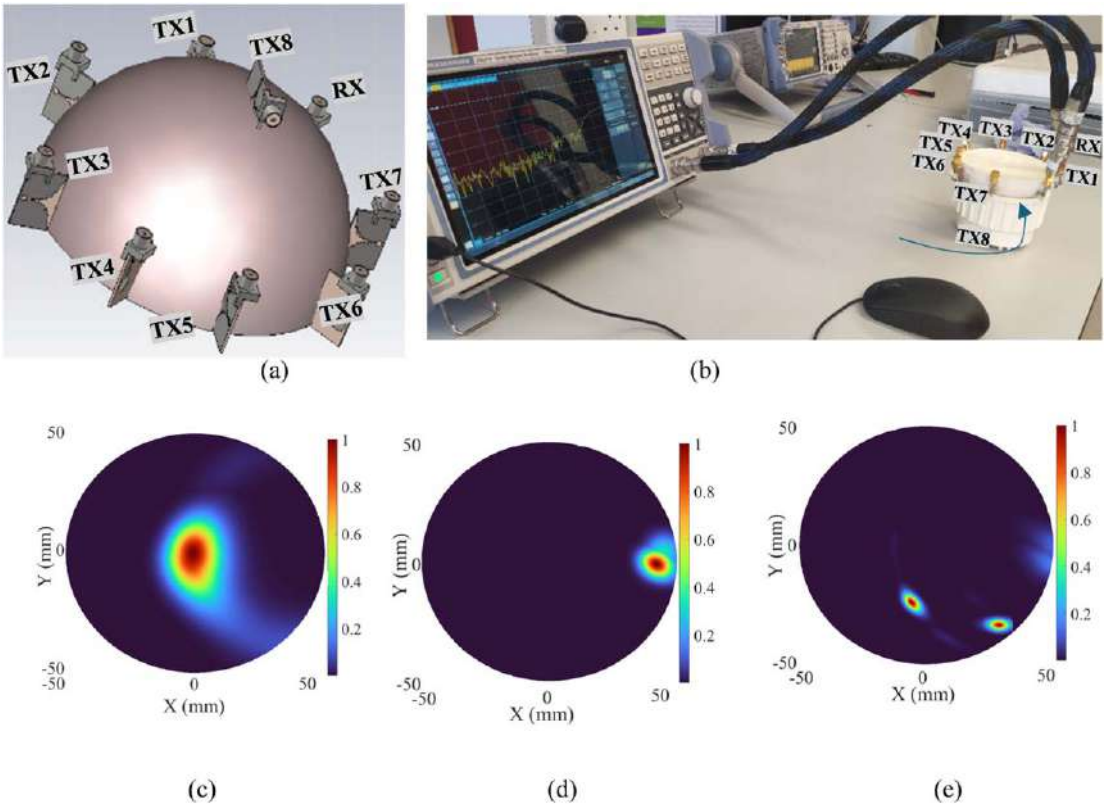

Figure 11. (a) BCD simulation, (b) BCD measurement setup using Ant. B array. Reconstructed 2D image using RTR algorithm from (c) one tumor at the center, (d) one tumor off center and (e) two centers off center.

signals. The use of UWB technology allows for a wide frequency range, enabling high-resolution detection of scattered signals caused by differences in tissue properties. The small dimensions of the antennas allow multiple elements to be arranged around the breast, gathering more data from various angles to improve the accuracy of the measurements. This setup is crucial for detecting abnormalities like tumors, which create distinct scattering patterns due to their different dielectric properties compared to healthy tissue. The measurement was performed using a vector network analyzer (VNA) with the model Rohde & Schwarz ZNLE18. As shown in figure 11(b), a semi-spherical container made of Polylactic Acid (PLA) is used to enclose the breast and skin. PLA is chosen because of its low dielectric constant, which is close to that of air, minimizing interference with the EM field distribution. This ensures that the scattered signals are not distorted by the container material, allowing for accurate measurements of how EM waves interact with the breast tissue. The EM waves sent by the antennas scatter when they encounter a target, such as a tumor, due to the contrast in dielectric properties between healthy and malignant tissue. The scattered signals are then collected by the receiving antennas for further analysis. Figure 11(b) shows the measurement setup in the presence of both skin and breast. The data are collected using manual switching. Thus, port one of the VNA is connected to the receiver antenna (RX) by cable; the second cable is connected to port two of the VNA; and then the cable is connected to the other eight transmitter antennas (TX1-TX8). It should be noted that for each measurement between the RX and TX, the other TXs are terminated as illustrated in figure 11(b).

One of the key benefits of this system is its ability to reduce clutter, which refers to noise and irrelevant reflections from healthy tissue. The microwave radar technique focuses on the highly scattered signals from tumors, which stand out due to their distinct scattering characteristics. The data collected from multiple angles are used to reconstruct an image of the breast tissue, highlighting potential tumors. This method provides high-resolution images and is non-invasive, making it a promising tool for early breast cancer detection.

Microwave medical imaging, particularly for breast cancer detection, offers several advantages. It provides a non-invasive and non-ionizing approach, making it safer than conventional imaging methods like x-rays. Its sensitivity to small tumors due to the dielectric contrast between healthy and malignant tissue allows for early detection. Moreover, the setup's multi-angle data collection and the PLA container's minimal interference enhance image resolution and measurement accuracy. This technique holds great potential for real-time monitoring and could significantly aid in early cancer diagnosis and treatment planning.

The measurement process is conducted after fabricating the skin and breast models. Although the dielectric properties of the breast (radius of 95 mm) and skin (radius of 100 mm, thickness of 5 mm) are already known, the dielectric properties of the fabricated skin and breast are measured and compared to the values reported in the literature before beginning the imaging reconstruction procedure.

Based on the procedure explained in [26, 51], the fabrication process for the skin is as follows:

1. **Prepare Solution**: Dissolve 0.2 g of p-toluic acid in 10 ml of n-propanol by heating with stirring. Mix this solution into 190 ml of deionized water at room temperature.
2. **Add Gelatin**: Stir in 34 g of gelatin. Cover the beaker and heat in a double boiler until the mixture becomes transparent and bubble-free (around 90 °C).
3. **Cool and Mix with Oil**: Cool the mixture to 50 °C, then mix it with oil (preheated to 50 °C) in another beaker. Stir vigorously while adding 0.56 ml of Tween 80 surfactant.
4. **Cool Further**: Continue cooling the emulsion to 40 °C, then add 2.16 g of formaldehyde solution. Further cool the mixture to 34 °C before pouring it into molds.
5. **Cross-linking**: Allow at least 5 days for the formaldehyde cross-linking process to complete.
6. **For Higher Oil Content** (**up to 80%**): Gradually add more oil (up to 80% by volume) with vigorous stirring, repeating the process until the desired oil content is achieved.

To fabricate the breast fat, which requires a dielectric constant of around 5.7, a similar process is followed. However, castor oil (with a dielectric constant of $\varepsilon r = 4.7$) is used, mixed with the gelation agent, and solidified to achieve the required dielectric properties around 5.7 which is the same as breast fat.

Following the simulation and measurement setup presented in figure 11 and the reflected and scattered signals from the antennas (Ant. B array), the 2D images of the tumor are reconstructed using the Robust Time Reverse (RTR) algorithm [40] as shown in figures 11(c)–(e). The nine antennas are selected to enhance the accuracy in detecting the tumor and remove the clutter effect considering the antenna array dimensions. In this scenario, the multi-static approach is utilized for image reconstruction of the tumor. However, only the received signals are considered when the antenna one sends and others receive. It is to save time and reduce the processing time of the imaging. To reconstruct the image from the scatters, the signal processing approach began with a sequential method akin to a traditional time-reversal (TR) algorithm, where signals containing and lacking targets were initially forwarded to ascertain differences. Subsequently, signals were reversed in time and propagated back to focus on specific target locations. After eliminating clutter and artifacts, the aim is to compute and isolate a tumor response from the overall field. This processing methodology holds significance as a target's response typically involves reflections from various layers within a sample, encompassing all irregularities. Therefore, the conventional TR algorithm is developed and expanded to RTR to reduce clutter and extract the hollow response from the entirety of scattering fields and signals. The RTR algorithm first subtracts the background effects (clutter from various sources, including side-lobe coupling). Then, removing early time content (ETC), multiplying scattered output, considering the time of arrival, and finally windowing the output signal to obtain the tumor response help with accurate detection. The proposed antenna's characteristics and the reconstructed images shown in figures 11(c)–(e) prove the antenna's ability to detect a tumor with a diameter of less than 10 mm in any location inside a breast.

Figures 11(c)–e) show the reconstructed images of breast tumors at different locations, as well as two tumors with 10 mm diameters inside the breast. These images were generated using signals captured from the measurement setup in figure 11(b), demonstrating the effectiveness of the proposed antenna array in detecting tumors. The antenna transmits high-frequency signals, such as microwaves, into the breast, which propagate through different tissues, each with unique dielectric properties. Tumors have distinct dielectric properties compared to healthy tissue, causing them to scatter the waves differently. The antenna array captures these scattered signals, and based on the variations in delay and intensity, reconstructs an image of the tissue. Since tumors scatter signals more strongly due to their higher dielectric constant, the system can detect tumors as small as 5 mm. Although some minor clutter appears around the tumor due to signal noise, it is not significant enough to mask the actual tumor image, affirming the antenna's precision in detecting tumors amidst background tissue.

5. Conclusion

This study exploits the new VNSPA theory to design more compact antennas than previously achieved. It also shows the importance of MATLAB optimization codes in achieving the proper ENSP that controls the

performance of the resultant antennas. As compared to previously designed UWB VTSA, new and improved reductions in size of 72.74 %, and 81.8 % are obtained for Antenna A and Antenna B, respectively. This has been achieved while maintaining matching and gain, with $S_{11} < -11.36$ dB and—10.21 dB and peak gain of 5.9 dBi and 6 dBi at 2.63–12.33 GHz and 3.16–14.34 GHz, respectively. Getting the required compactness based on the ENSP shape shows that the VTSA size can be reduced without degrading its performance, which is beneficial for modern wireless communication applications such as reader antennas in body area networks. This avoids the challenges and high cost of other techniques to reduce the antenna size while maintaining good performance. These compact designs are particularly advantageous for patient comfort and ease of integration into medical diagnostic equipment. The low SAR values achieved by Antenna B, along with its 30.58% smaller size and improved performance metrics of 13.24% bandwidth and 1.7% gain enhancement compared to Antenna A, make it suitable in this work for BCD using the UWB MI approach. The results demonstrate that Antenna B is an excellent candidate for high-resolution medical applications. The promising results of the ultra-compact Vivaldi antennas open new research and application opportunities. For example, the quality of the reconstructed images and the clutter removal can be improved using AI or an improved version of RTR. These antennas can be adapted for body area networks, IoT devices, and various medical imaging applications, including brain and cardiovascular diagnostics. Exploring these future prospects will push the boundaries of Vivaldi antenna technology, improving diagnostic methods, patient outcomes, and communication systems across various fields.

Acknowledgments

This study is supported via funding from Prince Sattam bin Abdulaziz University project number (PSAU/2024/R/1445) and Enterprise Ireland.

Data availability statement

The data cannot be made publicly available upon publication because the cost of preparing, depositing and hosting the data would be prohibitive within the terms of this research project. The data that support the findings of this study are available upon reasonable request from the authors.

Conflicts of interest

There are no conflicts of interest among the authors.

Appendix

The main function in the optimization code is as follows:

```
function opt_gamain=gamain_Zcoefficients(y)
****************************************
% Required design parameters %
**************************************
K=KTSP = KNSP= 50;
Er=3.55; h=0.813e-3; c=3e8; fc=6.85e9;
L_TSP=25e-3; % optimized value for VTSA
L_NSP =0.5* L_TSP; % LNSP=(1–0.5)* LTSP (Antenna A), LNSP=(1–0.6)* LTSP (Antenna B),
************************************************************
% Fixed parameters to guarantee the equivalence between LTSP and LNSP
************************************************************
W1=21.03e-3 % ; W2=0.3e-3; ra=0.17 %; A=0.5*W2;
%% The Frequency Range: UWB range
fmin=2e9; fmax=12e9; deltaf=0.025e9; % arbitrary increment and it is preferred to be small
f=fmin:deltaf:fmax;
Lambda0=c/fc;
%%%%%%%%%%%%%%%%%%%%%%%%%%%%%%%%%%%%%%%%%%%%%%%%%
for jj=1:1:length(f)
 abcd_NBS0=[1 0;0 1];% for ENSP
 abcd_TBS0=[1 0;0 1]; % for ETSP
```

```
for i=1:K
 X=((i-0.5)/(K));
W_TSP =A*exp(ra*X* L_TSP *1e3); % FOR ETSP
 Eeff=(Er+1)*0.5; % equations are from the Microstrip Lines and Strip Lines Book
 if W_TSP >(0.0015*Lambda0) & W_TSP <(0.075*Lambda0);
 LamdaS=Lambda0*(1.045–0.365*log(Er)+((6.3* W_TSP*h^−1*Er^0.945)/(238.64+100* W_
TSP *h^−1))-(0.148-(8.181*(Er+0.95))/(100*Er))*log(h/Lambda0));
Z_TSP=60+3.69*sin(((Er-2.22)*pi)/2.36)+133.5*log(10*Er)*sqrt(W_TSP /Lambda0)
+2.81*(1–0.011*Er*(4.48-log(Er))*( W_TSP
/h)*log(100*h*Lambda0^−1))+131.1*(1.028-log(Er))*sqrt(h/Lambda0)+12.48*(1+0.18*log(Er))*
(( W_TSP /h)/(sqrt(Er-2.06+0.85*( W_TSP /h)^2)));
 else
  LamdaS=Lambda0*(1.194–0.24*log(Er)-((0.621* W_TSP *Er^(0.835)*( W_TSP
/Lambda0)^0.48)/(1.344+ W_TSP *h^−1))−0.0617*(1.91-((Er+2))/(Er))*log(h/Lambda0));
 Z_TSP =133+10.34*(Er-1.8)^2+2.78*(2.96+(Er-1.582)^2)*(( W_TSP
*h^−1+2.32*Er-0.56)*((32.5–6.67*Er)*(100*h*Lambda0^−1)^2–1))^0.5-(684.45*h*Lambda0^−1)*
(Er+1.35)^2+13.23*((Er-1.722)*h*Lambda0^−1)^2;
 end
% ABCD parameters for ETSP
 A_TSB=cos(2*pi* L_TSP *f(jj)*sqrt(Eeff)/(c*K));
 D_TSB =cos(2*pi* L_TSP *f(jj)*sqrt(Eeff)/(c*K));
 B_TSB =1i*(Z_TSP)*sin(2*pi* L_TSP *f(jj)*sqrt(Eeff)/(c*K));
 C_TSB =1i*(( Z_TSP)^−1)*sin(2*pi*L_TSP*f(jj)*sqrt(Eeff)/(c*K));
 % Z(z) at the i'th section: the characteristic impedance of each section
W_NSB = W_TSB *(exp(y(1)*cos(2*pi*0*X)+y(2)*cos(2*pi*1*X)+y(3)*cos(2*pi*2*X)+y(4)*cos(2*pi*3*X)
+y(5)*cos(2*pi*4*X)+y(6)*cos(2*pi*5*X)+y(7)*cos(2*pi*6*X)+y(8)*cos(2*pi*7*X)+y(9)*cos(2*pi*8*X)+
y(10)*cos(2*pi*9*X)+y(11)*cos(2*pi*10*X)));% Based on equation 2 to find W_NSP
 Eeff=(Er+1)/2; %From the Microstrip Lines and Strip Lines Book
 if W_NSB >(0.0015*Lambda0) & W_NSB <(0.075*Lambda0);
 LamdaS=Lambda0*(1.045–0.365*log(Er)+((6.3* W_NSB *h^−1*Er^0.945)/(238.64+100* W_NSB
*h^−1))-(0.148-(8.181*(Er+0.95))/(100*Er))*log(h/Lambda0));
Z_NSP=60+3.69*sin(((Er2.22)*pi)/2.36)+133.5*log(10*Er)*sqrt(W_NSP/Lambda0)+2.81*
(1–0.01*Er*(4.48 log(Er))*(W_NSB/h)*log(100*h*Lambda0^1))+131.1*(1.028 log(Er))*sqrt(h/Lambda0)
+12.48*(1+0.18*log(Er))*((W_NSB /h)/sqrt(Er-2.06+0.85*( W_NSB /h)^2));
 else
  LamdaS=Lambda0*(1.194-0.24*log(Er)-((0.621*W_NSP*Er^(0.835)*( W_NSB /Lambda0))/(1.344+
W_NSB *h^−1))−0.617*(1.91-((Er+2))/(Er))*log(h/Lambda0));
 Z_NSB =133+10.34*(Er-1.8)^2++2.78*(2.96+(Er-1.582)^2)*((W_NSB *h^−1+
2.32*Er-0.56)*((32.5–6.67*Er)*(100*h*Lambda0^−1)^2-1))^0.5-(684.45*h*Lambda0^−1)*(Er+1.35)^2+
13.23*((Er-1.722)*h*Lambda0^−1)^2;
 end
 A_NSB=cos(2*pi* L_NSP *f(jj)*sqrt(Eeff)/(c*K));
 D_NSB =cos(2*pi* L_NSP *f(jj)*sqrt(Eeff)/(c*K));
 B_NSB =1i*(Z_NSP)*sin(2*pi* L_NSP *f(jj)*sqrt(Eeff)/(c*K));
 C_NSB =1i*((Z_NSP)^−1)*sin(2*pi* L_NSP *f(jj)*sqrt(Eeff)/(c*K));
 abcd_NBS0=[1 0;0 1];% for ENSP
 abcd_TBS0=[1 0;0 1]; % for ETSP
abcd_TSP0=[A_TSB B_TSB;C_TSB D_TSB];
 abcd_TSP=abcd_TSP*abcd_TSP0;
abcd_NSP0=[A_NSB B_NSB;C_NSB D_NSB];

abcd_NSP=abcd_NSP*abcd_NSP0;
 end
error(jj)=0.25*((abs(abcd_NSP(1,1)-abcd_TSP(1,1)))^2+( Z_NSP ^−2)*
(abs(abcd_NSP(1,2)-abcd_TSP(1,2)))^2+(Z_NSP^2)*(abs(abcd_NSP(2,1)abcd_TSP(2,1)))^2+(abs
(abcd_NSP(2,2)-abcd_TSP(2,2)))^2);
 error1=0;
 error1=error(jj)+error1;
 error=sqrt((1/(length(f))*error1));
```

```
end
opt_gamain=max(error);
```

Note: After getting the optimized error, this will be called in the main built in function (fmincon) to get the required Fourier series coefficients (Cn) values in equation 2, according to the required constraints. After getting these coefficients, the NSP profiles can be drawn based on the variable width.

ORCID iDs

Sahar Saleh https://orcid.org/0000-0002-0015-5972
Tale Saeidi https://orcid.org/0000-0001-5165-5814
Faroq Razzaz https://orcid.org/0000-0001-9292-6043
Ayman A Althuwayb https://orcid.org/0000-0001-5160-5016

References

[1] Zhurbenko V 2010 *Passive Microwave Components and Antennas* (BoD–Books on Demand)
[2] Jarufe C, Rodriguez R, Tapia V, Astudillo P, Monasterio D, Molina R, Mena F P, Reyes N and Bronfman L 2018 Optimized corrugated tapered slot antenna for mm-wave applications *IEEE Trans. Antennas Propag.* **66** 1227–35
[3] Islam M T, Islam M T, Samsuzzaman M, Arshad H and Rmili H 2020 Metamaterial loaded nine high gain vivaldi antennas array for microwave breast imaging application *IEEE Access* **8** 227678–89
[4] Won H, Hong Y, Choi M, Lee W, Taylor D, Chung C and Lee J 2023 Miniaturized tapered-slot ultra-wideband Vivaldi antenna for ice sounding radar *Microw Opt Technol Lett* **65** 2808–13
[5] Guruswamy S, Chinniah R and Thangavelu K 2019 A printed compact UWB Vivaldi antenna with hemi cylindrical slots and directors for microwave imaging applications *AEU-International Journal of Electronics and Communications* **110** 152870
[6] Cheng H, Yang H, Li Y and Chen Y 2020 A compact vivaldi antenna with artificial material lens and sidelobe suppressor for GPR applications *IEEE Access* **8** 64056–63
[7] Czyzewski M, Szczepaniak Z and Slowik A 2022 Miniaturized vivaldi antenna for moist estimation in masonry walls 2022*24th International Microwave and Radar Conference (MIKON)* (IEEE) p 1–4
[8] Zhang K, Tan R, Jiang Z H, Huang Y, Tang L and Hong W 2022 A compact, ultrawideband dual-polarized vivaldi antenna with radar cross section reduction *IEEE Antennas Wirel. Propag. Lett.* **21** 1323–7
[9] Kapoor A, Kumar P and Mishra R 2017 High gain modified Vivaldi vehicular antenna for IoV communications in 5G network *Heliyon* e09336
[10] Abushakra F, Jeong N, Elluru D N, Awasthi A K, Kolpuke S, Luong T, Reyhanigalangashi O, Taylor D and Prasad Gogineni S 2022 A miniaturized ultra-wideband radar for UAV remote sensing applications *IEEE Microwave Wirel. Compon. Lett.* **32** 198–201
[11] Anguera J, Andújar A, Huynh M-C, Orlenius C, Picher C and Puente C 2013 Advances in antenna technology for wireless handheld devices *Int J Antennas Propag* **2013** 838364
[12] Saleh S, Jamaluddin M H, Razzaz F, Saeed S M, Timmons N and Morrison J 2023 Compactness and performance enhancement techniques of ultra-wideband tapered slot antenna: a comprehensive review *Alexandria Engineering Journal* **74** 195–229
[13] Yeo J 2022 Compact, gain-enhanced , linearly tapered slot antenna with a combined director using a strip director and double-sided metamaterial loading for UWB applications **127** 263–77
[14] Kim S-W and Choi D-Y 2016 Implementation of rectangular slit-inserted ultra-wideband tapered slot antenna *Springerplus* **5** 1387
[15] Zhang P and Li J 2017 Compact UWB and low-RCS Vivaldi antenna using ultrathin microwave-absorbing materials *IEEE Antennas Wirel. Propag. Lett.* **16** 1965–8
[16] Ren J, Fan H, Tang Q, Yu Z, Xiao Y and Zhou X 2022 An ultra-wideband vivaldi antenna system for long-distance electromagnetic detection *Applied Sciences* **12** 528
[17] Gao P, Dou W, Wang F and Chen X 2016 The miniaturization design of tapered slot antenna for wideband applications *Asia-Pacific Microwave Conference Proceedings, APMC* **2** 2–4
[18] Tang Y, Cao X, Song Y, Jidi L, Lan J and Yu H 2018 A design of high-gain vivaldi antenna loaded with antipodal structure and slotting correction *2018 IEEE MTT-S International Wireless Symposium (IWS)* (IEEE) p 1–3
[19] Saleh S, Ismail W, Abidin I S Z, Jamaluddin M H, Bataineh M H and Alzoubi A S 2022 Compact UWB vivaldi tapered slot antenna *Alexandria Engineering Journal* **61** 4977–94
[20] Wang J, Liu J, Fan Y and Bai Y 2023 A novel Vivaldi antenna for UWB detection *Microw Opt Technol Lett* **65** 826–43
[21] Seo J, Kim J H and Oh J 2020 Semicircular patch-embedded Vivaldi antenna for miniaturized UWB radar sensors *Sensors* **20** 5988
[22] Navarro-Méndez D V, Carrera-Suárez L F, Antonino-Daviu E, Ferrando-Bataller M, Baquero-Escudero M, Gallo M and Zamberlan D 2015 Compact wideband vivaldi monopole for LTE mobile communications *IEEE Antennas Wirel. Propag. Lett.* **14** 1068–71
[23] Saleh S, Ismail W, Abidin I S Z, Bataineh M H and Al-Zoubi A S 2022 Novel compact UWB Vivaldi nonuniform slot antenna with enhanced bandwidth *IEEE Trans. Antennas Propag.* **70** 6592–603
[24] Ghorbian M and Ghorbian S 2023 Usefulness of machine learning and deep learning approaches in screening and early detection of breast cancer *Heliyon* **9** e22427
[25] Saleh S, Saeidi T and Timmons N 2024 Simple compact UWB Vivaldi antenna arrays for breast cancer detection *Telecom* **5** 312–32
[26] Alani S, Zakaria Z, Saeidi T, Ahmad A, Imran M A and Abbasi Q H 2021 Microwave imaging of breast skin utilizing elliptical uwb antenna and reverse problems algorithm *Micromachines (Basel)* **12** 647
[27] Mahmood S N, Ishak A J, Jalal A, Saeidi T, Shafie S, Soh A C, Imran M A and Abbasi Q H 2021 A bra monitoring system using a miniaturized wearable ultra-wideband MIMO antenna for breast cancer imaging *Electronics (Basel)* **10** 2563
[28] Vijaykumar K, Baskaran M, Gayathri V and Gayathri P 2020 Design of 4 × 4 antenna array for breast cancer detection *Analog Integr. Circuits Signal Process.* **105** 395–406
[29] Slimi M, Jmai B, Dinis H and Gharsallah A 2022 Microwave imaging for breast tumor detection using a CPW antenna *Indian J Sci Technol* **15** 554–60

[30] Dey A B and Arif W 2022 Design and analysis of a CPW-fed flexible ultrawideband antenna for microwave imaging of breast cancer *International Journal of RF and Microwave Computer-Aided Engineering* **32** e23262
[31] Li H, Zhang H, Kong Y and Zhou C 2022 Flexible dual-polarized UWB antenna sensors for breast tumor detection *IEEE Sens. J.* **22** 13648–58
[32] Syed A, Sheikh M, Islam M T and Rmili H 2022 Metamaterial-loaded 16-printed log periodic antenna array for microwave imaging of breast tumor detection *Int J Antennas Propag* **2022** 4086499
[33] Elsheakh D N, Mohamed R A, Fahmy O M, Ezzat K and Eldamak A R 2023 Complete breast cancer detection and monitoring system by using microwave textile based antenna sensors *Biosensors (Basel)* **13** 87
[34] Subrahmanyam G V and Krishna K S R 2024 A novel compact semicircular defected ground structure ultrawideband monopole antenna integrated with Ku band for breast cancer detection *Int. J. Commun. Syst.* **37** e5632
[35] Kaur G and Kaur A 2022 C' shaped dual polarized dielectric resonator antenna for the microwave imaging of breast tumor using beam-forming algorithms *Int. J. RF Microwave Comput. Aided Eng.* **32** 1–20
[36] Slimi M, Jmai B, Dinis H, Gharsallah A and Mendes P M 2022 Metamaterial vivaldi antenna array for breast cancer detection *Sensors* **22** 3945
[37] Asok A O, Tripathi A and Dey S 2023 Systematic performance evaluation for the detection of breast tumors with sinusoidal corrugated antipodal vivaldi antennas utilizing DAS and It-DAS methodologies *Progress in Electromagnetics Research C* **137**
[38] Zerrad F, Taouzari M, Makroum E M, Aoufi J, El, Qanadli S D, Karaaslan M, Al-Gburi A J A and Zakaria Z 2023 Microwave imaging approach for breast cancer detection using a tapered slot antenna loaded with parasitic components *Materials* **16** 1496
[39] Saleh S, Ismail W, Zainal Abidin I S, Jamaluddin M H, Al-Gailani S A, Alzoubi A S and Bataineh M H 2020 Nonuniform compact Ultra-Wide Band Wilkinson power divider with different unequal split ratios *J. Electromagn. Waves Appl.* **34** 154–67
[40] Saeidi T, Ismail I, Mahmood S N, Alani S and Alhawari A R H 2020 Microwave imaging of voids in oil palm trunk applying UWB antenna and robust time-reversal algorithm *J Sens* **2020** 1–21
[41] Balanis C A 2016 *Antenna Theory: Analysis and Design* (wiley)
[42] Khalaj-Amirhosseini M 2006 Wideband or multiband complex impedance matching using microstrip nonuniform transmission lines *Jpier.Org* **66** 15–25
[43] Anon fmincon - Find minimum of constrained nonlinear multivariable function - MATLAB - MathWorks United Kingdom (https://uk.mathworks.com/help/optim/ug/fmincon.html)
[44] Garg R, Bahl I and Bozzi M 2013 *Microstrip Lines and Slotlines* (Artech house)
[45] Pozar D M 2012 *Microwave Engineering* 4th edn (Wiley) (http://mwl.diet.uniroma1.it/people/pisa/RFELSYS/MATERIALE%20INTEGRATIVO/BOOKS/Pozar_Microwave%20Engineering(2012).pdf)
[46] Sayed A, Ghonam R S and Zekry A 2015 Design of a compact dual band microstrip antenna for Ku-Band applications *Int. J. Comput. Appl.* **115** 11–4
[47] Elsheakh D M N, Eltresy N A and Abdallah E A 2017 Ultra wide bandwidth high gain Vivaldi antenna for wireless communications *Progress In Electromagnetics Research* **69** 105–11
[48] AlFares B, AlJabr A, Zainalabedin M, AlMuzain M, Saleh G and AlHashim M 2021 Heterogenous breast phantom with carcinoma for ionizing machines *2021 IEEE Int. IOT, Electronics and Mechatronics Conf. (IEMTRONICS)* (IEEE) 1–6
[49] White S A, Landry G, Van Gils F, Verhaegen F and Reniers B 2012 Influence of trace elements in human tissue in low-energy photon brachytherapy dosimetry *Phys. Med. Biol.* **57** 3585–96
[50] Ruvio G, Solimene R, Cuccaro A, Fiaschetti G, Fagan A J, Cournane S, Cooke J, Ammann M J, Tobon J and Browne J E 2020 Multimodal breast phantoms for microwave, ultrasound, mammography, magnetic resonance and computed tomography imaging *Sensors* **20** 2400
[51] Lazebnik M, Madsen E L, Frank G R and Hagness S C 2005 Tissue-mimicking phantom materials for narrowband and ultrawideband microwave applications *Phys. Med. Biol.* **50** 4245